Deep-Sea Research I 79 (2013) 106–121

Contents lists available at SciVerse ScienceDirect

Deep-Sea Research I

journal homepage: www.elsevier.com/locate/dsri

Long-term trends of upwelling and impacts on primary productivity in the Alaskan Beaufort Sea

Robert S. Pickart [a,*], Lena M. Schulze [a], G.W.K. Moore [b], Matthew A. Charette [a], Kevin R. Arrigo [c], Gert van Dijken [c], Seth L. Danielson [d]

[a] Woods Hole Oceanographic Institution, Woods Hole, MA 02543, USA
[b] Department of Physics, University of Toronto, Toronto, ON, Canada
[c] Department of Environmental Earth System Science, Stanford University, Stanford, CA, USA
[d] University of Alaska, Fairbanks, AK, USA

ARTICLE INFO

Article history:
Received 2 November 2012
Received in revised form
2 May 2013
Accepted 8 May 2013
Available online 23 May 2013

Keywords:
Long-term wind trends
Upwelling trends
Nitrate flux
Primary production

ABSTRACT

Using a previously established wind proxy for upwelling along the North Slope of Alaska, we examine the interannual to decadal variability in upwelling as well as the climatological monthly trends. The ability of the upwelling to trigger phytoplankton blooms via upward nitrate flux from the halocline is then investigated using data from a moored array together with the proxy. The 70-year record of wind speed from the Barrow, Alaska meteorological station (1941–2010) reveals that strong upwelling events – lasting at least 4 days and exceeding 10 m/s during the storm – occur throughout the year. On average there are 9–10 upwelling events per year, and the number and strength of events has increased over the last 25 years. The low-frequency variability in the upwelling co-varies with previously documented Arctic climate trends, but there is no significant correlation with various high latitude atmospheric indices. There are two seasonal peaks in the occurrence of upwelling, in May and November. The role of the Beaufort High and Aleutian Low in driving the upwelling is investigated using NCEP reanalysis fields. Fluctuations in both of these centers of action contribute to the enhanced winds, and the location of the Aleutian Low storm track plays a key role in the seasonal variability of the upwelling. The upward nitrate flux due to storms in the open water period can account for new primary production that is on par with carbon fixed during the summer growing season in the absence of storms. Evidence from satellite ocean color data of such wind-induced phytoplankton blooms is presented.

1. Introduction

Upwelling is a ubiquitous process along the Alaskan Beaufort Sea shelfbreak and slope, driven by the predominantly easterly winds in the region. These winds arise due to the enhanced sea-level pressure gradient between two centers of action: the Beaufort High and the Aleutian low. More specifically, distinct upwelling events can be triggered by Aleutian low storms passing far to the south (Pickart et al., 2009a) as well as by fluctuations in the Beaufort High (Mathis et al., 2012). The oceanographic response to these easterly wind bursts, which can last for many days, is pronounced and represents an effective mechanism for shelf-basin exchange. Pickart et al., (2013); demonstrated that a single (strong) upwelling storm in autumn can flux enough heat offshore to melt one meter of ice over an area the size of the Alaskan Beaufort shelf. In addition, the quantity of freshwater transported offshore can account for a significant fraction of the observed year-to-year variability in freshwater content of the Beaufort Gyre (Pickart et al., 2013; Proshutinsky et al., 2009). This is in line with the findings of Yang (2006) who used historical wind and ice information to investigate the seasonal variability of the Beaufort Gyre.

The general circulation of the Alaskan Beaufort Sea consists of wind-driven westward flow in the interior (the southern arm of the Beaufort Gyre) and a buoyancy-driven shelfbreak current (Fig. 1), which is referred to as the Beaufort shelfbreak jet or western Arctic boundary current (Nikolopoulos et al., 2009). On the inner shelf the flow is weaker and more variable (Aagaard and Roach, 1990; Kasper and Weingartner, 2012). The shelfbreak jet advects Pacific-origin water eastward (Fig. 1), and varies from a surface-intensified jet in late-summer/early-fall to a bottom-intensified current over the remainder of the year (Nikolopoulos et al., 2009). The summertime jet advects warm (4–6 °C) Alaskan Coastal Water, while the bottom-intensified current transports different water masses seasonally: In spring the water is generally very cold (near the freezing point) newly-ventilated winter water (Spall et al., 2008); in early-summer

* Corresponding author. Tel.: +1 508 289 2858; fax: +1 508 457 2181.
E-mail address: rpickart@whoi.edu (R.S. Pickart).

0967-0637/$ - see front matter © 2013 Elsevier Ltd. All rights reserved.
http://dx.doi.org/10.1016/j.dsr.2013.05.003

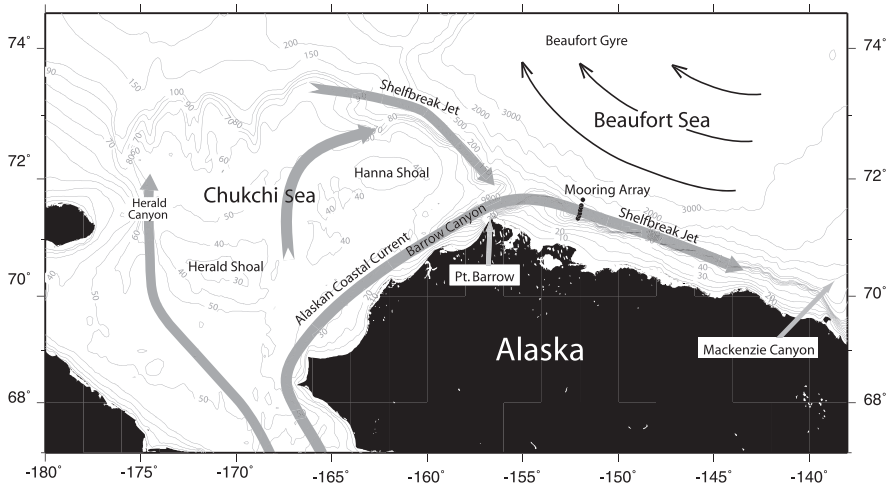

Fig. 1. Schematic of the major currents of the Chukchi and Beaufort Seas and geographical place names. The solid circles indicate the locations of the Beaufort slope moorings.

it is warmer (0–2 °C) Chukchi Summer Water (von Appen and Pickart, 2012); and in late-fall and winter it is cold (−1.5–0 °C) winter-remnant water (Nikolopoulos et al., 2009).

When the easterly winds exceed approximately 4 m/s, the shelfbreak jet tends to reverse to the west and upwelling commences roughly half a day later (Schulze and Pickart, 2012). The associated secondary (cross-stream) circulation during the event transports the Pacific water offshore in the surface layer, and brings water from the interior basin upwards and onshore (Pickart et al., 2011). Upwelling can occur during any month of the year and in nearly all ice conditions. Schulze and Pickart (2012) demonstrated that the oceanographic response is strongest when there is partial ice concentration. This is due to effective transfer of momentum from the wind to the water column via the freely-moving ice keels and ridges (McPhee, 1980; Pickart et al., 2013). Although more muted, upwelling occurs even with 100% ice cover and when landfast ice is located on the shelf (Schulze and Pickart, 2012). Analysis of the dynamics of an autumn storm event (Pickart et al., 2013) suggests that non-linear momentum flux divergence augments the wind forcing, while the alongstream pressure gradient that builds during the storm helps to re-establish the eastward-flowing shelfbreak jet as the winds subside. Shelf waves generated by the winds influence the water column in regions away from the direct influence of the atmosphere (e.g. Aagaard and Roach, 1990; Carmack and Kulikov, 1998; Pickart et al., 2011).

In addition to changing the physical state of the Beaufort Sea, upwelling has the potential to impact various aspects of the ecosystem as well. For example, outgassing of CO_2 can occur along with mineral undersaturation as subsurface waters are brought to the surface (Mathis et al., 2012), and zooplankton can be advected laterally which can affect cetacean feeding patterns (Ashjian et al., 2010; Walkusz et al., 2012). Another potential impact pertains to the distribution of nutrients. The cold Pacific-origin winter water that flows northward through Bering Strait into the Chukchi Sea contains elevated concentrations of silicate, nitrate, nitrite and phosphate. This fuels primary productivity on the Chukchi shelf (e.g. Sambrotto et al., 1984; Hansell et al., 1993; Hill and Cota, 2005; Hill et al., 2005) which in turn leads to enhanced benthic activity (Grebmeier, 1993). However, much of the high-nutrient dense Pacific water ends up in the interior Canada Basin within the upper halocline. Hence there is a large reservoir of nutrients residing just offshore of the shelfbreak which can potentially be tapped via upwelling. Winter water is commonly upwelled in Barrow Canyon (Pickart and Fratantoni, 2011), which may help explain why the canyon has such high production rates (Hill and Cota 2005) and is elevated in benthic biomass (Grebmeier, 2012). However, since upwelling takes place along the entire Beaufort slope, there may be similar impacts over a much broader area.

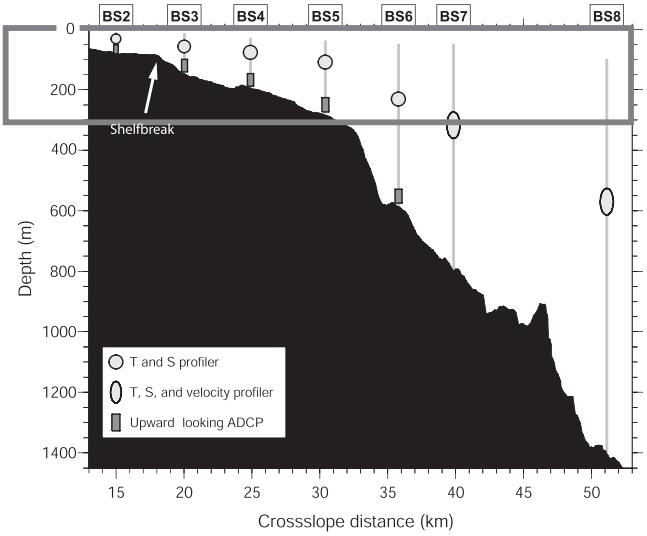

Fig. 2. The SBI mooring array. The location and name of each mooring is marked at the top and instruments used are listed in the bottom left corner. The grey box indicates the portion of the water column addressed in this study. The bottom topography is from echosounder measurements taken during the program.

While the recent studies on upwelling in the Beaufort Sea have enhanced our understanding of this process, there are many remaining issues to be addressed regarding both the atmospheric forcing and the oceanographic and ecosystem response. This paper investigates two different but related aspects of upwelling. First, we aim to learn more about the nature and long-term variability of the atmospheric forcing using a 70-year timeseries (1941–2010) of wind measured at the meteorological station in Barrow, Alaska (Fig. 1). This timeseries nicely captures storm events that drive upwelling along the North Slope (e.g. Nikolopoulos et al., 2009; Pickart et al., 2009a). Previous in-situ measurements from a two-year mooring array deployed across the Beaufort shelf and slope, in conjunction with the Barrow weather station wind data, have allowed us to establish an empirical relationship between wind strength and the occurrence of upwelling (Schulze and Pickart, 2012). Here we use this relationship to identify upwelling storms over the full 70-year extent of the wind timeseries in order to investigate seasonal and long-term trends in the atmospheric

forcing. The second aim of the paper is to assess the potential impact of upwelling on primary productivity via the delivery of nutrients to the euphotic zone. This is accomplished using the mooring data in conjunction with shipboard nutrient data. The long wind timeseries helps us to gauge the importance of this process and how it varies in time. The overall goal of the study is to enhance our understanding of both the forcing and impacts of the upwelling that is so prevalent in the Beaufort Sea, with an eye towards assessing how this process might change in a warming climate.

2. Data and methods

2.1. Mooring data

From August 2002–September 2004 a mooring array was deployed across the Beaufort shelfbreak and continental slope at 152°W (Fig. 1), as part of the Western Arctic Shelf-Basin Interactions (SBI) program. The array included seven moorings (BS2–BS8) with a lateral spacing of 5–7 km for the inner six moorings and roughly 10 km for the seaward-most mooring (Fig. 2). The deployment was interrupted by a short turnaround in September 2003. The reader is referred to Nikolopoulos et al. (2009) and Spall et al. (2008) for a description of the array as well as information concerning data quality and measurement accuracies.

At each site, hydrographic variables were measured using a conductivity-temperature-depth (CTD) moored profiler providing vertical traces 2–4 times a day with a resolution of 2 m. The top float of each mooring was located at roughly 45 m depth to avoid potential damage to the mooring by ice keels. As such, the profiler data are limited to the part of the water column deeper than 45 m. Upward-facing acoustic Doppler current profilers (ADCPs) at the base of moorings BS2–BS6 provided hourly profiles of velocity with a vertical resolution of 5–10 m. These profiles have a blanking region near the surface that ranges from 8 m at BS2 to 45 m at BS6. The outer two moorings (BS7 and BS8) were equipped with acoustic travel-time current meters, but are not considered in this study. The ADCP velocity data were de-tided and then rotated into an alongstream/cross-stream coordinate frame. In between storms, when the flow of the shelfbreak jet is predominantly eastward, we used a rotation angle of 125ºT which is approximately aligned with the topography of the continental slope to the west (upstream) of the array (see Nikolopoulos et al., 2009). During storms, when the shelfbreak jet is reversed, the primary direction of the flow varied from event to event, and a rotation angle was objectively chosen for each individual storm (see Schulze and Pickart (2012) for details). The hydrographic data were used to construct vertical sections of potential temperature, salinity and potential density every 6 hours as described in Spall et al. (2008), and the ADCP data were used to construct hourly vertical sections of alongstream and cross-stream velocity (see Nikolopoulos et al., 2009).

2.2. Meteorological timeseries

Meteorological data from the Barrow Post-Rogers Airport were obtained from the National Climate Data Center (NCDC, http://www.ncdc.noaa.gov/). Barrow is located roughly 150 km to the west of the mooring array (Fig. 1), and previous studies have demonstrated that the winds at this location are generally a good proxy for those at the array site (Nikolopoulos et al., 2009; Pickart et al., 2011). Wind speed and direction measurements began in 1930 with twice-daily observations; six observations per day began in 1941, and an hourly observation schedule began in mid-1946. As such, we consider the 70-yr period from 1941 to 2010. The Barrow station location or sensor height changed ten times since 1941 (see the station history at the NOAA Multi-Network Metadata System https://mi3.ncdc.noaa.gov/mi3qry/), and the data resolution and data quality has varied through the years with different observers and different instrumentation systems in use. This must be kept in mind when trying to discern subtle variations. However, the strength of the signals discussed in the present study, and the averaging employed, indicates that our results are robust. This is supported by our error estimates which reveal large signal to noise ratios.

After obtaining the data from NCDC we converted the wind speed and direction into vector timeseries and subjected them to a detailed manual inspection process through which we removed spikes and obviously contaminated records (e.g. stuck sensor readings). Overall, the data quality was very good and only minimal hand editing was needed or applied, although a number of erroneous zero wind speed readings were removed. Also, several tens of high wind speed events (mostly from the 1970s and 1980s) were discarded. These were identified by instances of the otherwise smoothly changing vector timeseries undergoing large (e.g. 15–30 m/s) instantaneous jumps that returned to nearly the original level at the following time step. To fill in short data gaps that exist in the original dataset or as a result of the de-spiking, the data were linearly interpolated to the beginning of each observation hour. Interpolated records were retained only for those that fell within observational data gaps shorter than six hours.

During the 70-year time period only 1943 had significantly fewer data points than other years. This is due to two data gaps (1 Apr–31 May and 1 Sep–31 Oct), that are likely associated with wartime interruptions of observation. Since this study is focused on seasonal and long-term trends of strong wind events (see Section 3), we are confident that these gaps do not bias the results. Nikolopoulos et al. (2009) determined that the direction of wind most strongly correlated to the water column flow is along 105 °T, which is approximately aligned with the Beaufort coast. We rotated the wind data accordingly, and, from here on, unless explicitly stated otherwise the wind speed corresponds to the alongcoast component. Negative values refer to easterly winds.

2.3. Reanalysis fields

To investigate various aspects of the broad-scale atmospheric circulation and forcing we used reanalysis fields from the National Centers for Environmental Prediction (NCEP). This is a 6-h global product with a lateral resolution of 2.5° for sea-level pressure, and approximately 1.9° for 10 m winds starting in 1948 and continuing to the present (Kalnay et al. 1996). As such, it represents the longest continuously updated reanalysis dataset that assimilates both surface and upper-air data. It employs the global data assimilation and forecast model that was operational at NCEP in 1994. These reanalysis fields were used by Pickart et al. (2009a) in their study of storm systems that influence the Beaufort slope. Also, Pickart et al. (2011) demonstrated that the NCEP winds in the vicinity of Barrow during an upwelling event were in good agreement with those measured at the meteorological station. Finally, the NCEP Reanalysis has been used to document the characteristics, inter-annual variability, and trends in the Beaufort High (Serreze and Barrett, 2011; Moore, 2012).

2.4. Shipboard hydrographic and nitrate data

During the recovery cruise of the mooring array in September 2004, a high-resolution CTD/water sample section was occupied adjacent to the array. The CTD measurements were carried out with a SeaBird 911+ instrument with dual temperature and conductivity sensors on a rosette frame with 24 10-l Niskin bottles.

The temperature sensors underwent laboratory calibrations before and after the cruise, and the conductivity sensors were calibrated using in-situ water sample salinity data. The accuracy of the temperature measurements is 0.001 °C. For salinity, the accuracy is 0.002 for the deep water and 0.007 for stations on/near the shelf (Zimmermann and McKee, 2004). Nitrate+nitrite (NO_3^-+NO_2^-, hereafter referred to as nitrate) was measured during the cruise at discrete water sample depths, typically every 25 m spanning the halocline with increased vertical resolution in the vicinity of the shelf. The analysis was done on a Seal Analytical continuous-flow AutoAnalyzer 3 (see Gordon et al., 1992; Hager et al., 1972; Atlas et al., 1971; and Kerouel and Aminot, 1997 for a description of the methods). The expected detection limit is 0.05 μmol/L.

2.5. Ocean color satellite imagery

Satellite-derived chlorophyll *a* concentrations used in the study were based on Level 2 MODIS/Aqua ocean color data (OC3 algorithm, Reprocessing 2012.0) and were retrieved from www.oceancolor.gsfc.nasa.gov. The scenes were re-projected (polar stereographic) using the SeaDAS image processing software (www.seadas.gsfc.nasa.gov). Turbid water pixels were identified based on the complimentary Level-2 TURBIDW processing flag.

3. Physical aspects of upwelling

3.1. Trends of wind and upwelling

Before investigating upwelling events, it is instructive to consider aspects of the overall wind speed. The average wind speed over the full 70-yr record is -1.8 ± 0.05 m/s. While the range in annually averaged wind speed is roughly 3 m/s, the prevailing winds are out of the east—i.e. upwelling favorable (Fig. 3a). Hence, the Beaufort shelfbreak jet consistently opposed the wind during every one of the 70 years. The average value for each of the decades is indicated by the dashed lines in Fig. 3a. One sees that the wind has increased over the last two decades (to values larger than any of the previous decades). However, the interannual variability has been quite pronounced during the most recent decade.

The climatological monthly mean wind speed (Fig. 4a) indicates that there are two seasonal peaks of enhanced easterly wind, one in May and a second in the fall (Oct/Nov). The latter peak conforms to the results of Pickart et al. (2009a), who demonstrated that Aleutian low storms are often extensive enough to result in easterly winds in the southern Beaufort Sea. Since the Aleutian low sea-level pressure signal is deeper in the fall/winter (e.g. Favorite et al., 1976; Pickart et al., 2009b), there should be a corresponding increase in the easterlies along the North Slope of Alaska. The second peak in easterly wind speed in May was unexpected and is addressed further below. We note that the same seasonal trend in wind strength as seen in Fig. 4a is also present in the vector-averaged wind speed, with little variation in direction from month to month (not shown).

To analyze the frequency and trends of upwelling events over the last 70 years, we use an empirical relationship established by Schulze and Pickart (2012) who investigated the ability to predict the occurrence of upwelling along the Beaufort slope using the Barrow wind data alone. In particular, Schulze and Pickart (2012) examined the characteristics of all of the upwelling events that took place over the two-year time period of the SBI mooring array (45 events total), and compared this to the atmospheric forcing. An upwelling event was identified according to the following three criteria: (1) easterly wind speed at Barrow exceeding 4 m/s, (2) significant reversed (westward) flow in the shelfbreak jet, and (3) an increase in salinity in the near-bottom layer in the vicinity of the shelfbreak that exceeds the monthly mean. The reader is referred to Schulze and Pickart (2012) for a more detailed discussion of these criteria. Following this, the number of easterly wind bursts measured at the Barrow weather station was compared to those wind events that actually resulted in upwelling as detected by the mooring array. The results indicated that approximately 65% of wind bursts at Barrow exceeding 4 m/s result in upwelling, while approximately 95% of winds exceeding 10 m/s drive upwelling. The 100% threshold was reached for wind bursts exceeding 11 m/s. The reader is referred to figure 15 in Schulze and Pickart (2012) which shows the full wind-upwelling relationship.

Using this empirical relationship, we analyzed the 70-yr Barrow wind record and identified all storms that lasted at least 4 days and exceeded 10 m/s at some point during the storm. A length of 4-days was chosen because phytoplankton take approximately this long to respond to an enhanced nutrient supply, which is investigated in the second part of the paper (Section 4). We revealed 665 likely upwelling events during the

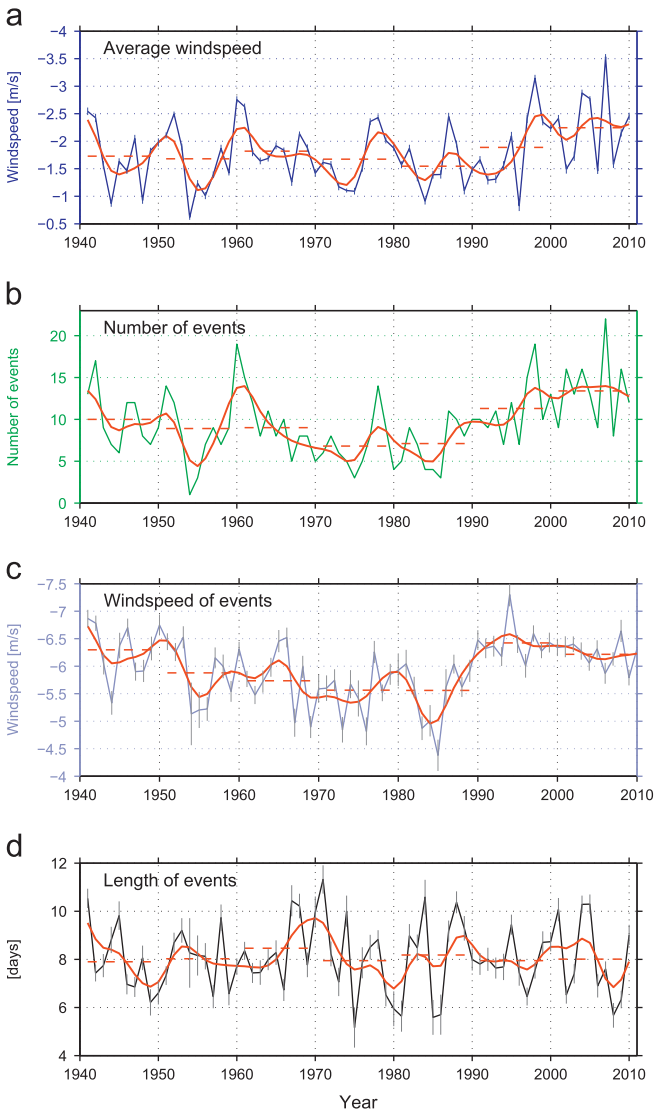

Fig. 3. (a) Annually averaged wind speed along 105°T (blue curve, including the standard error) and 7-yr lowpass (red curve) measured by the Barrow meteorological station. The red dashed lines denote the decadal averages. (b) Number of upwelling events in each year. (c) Average wind speed of the upwelling events during each year. (d) Average length of the upwelling events. (For interpretation of the references to color in this figure legend, the reader is referred to the web version of this article.)

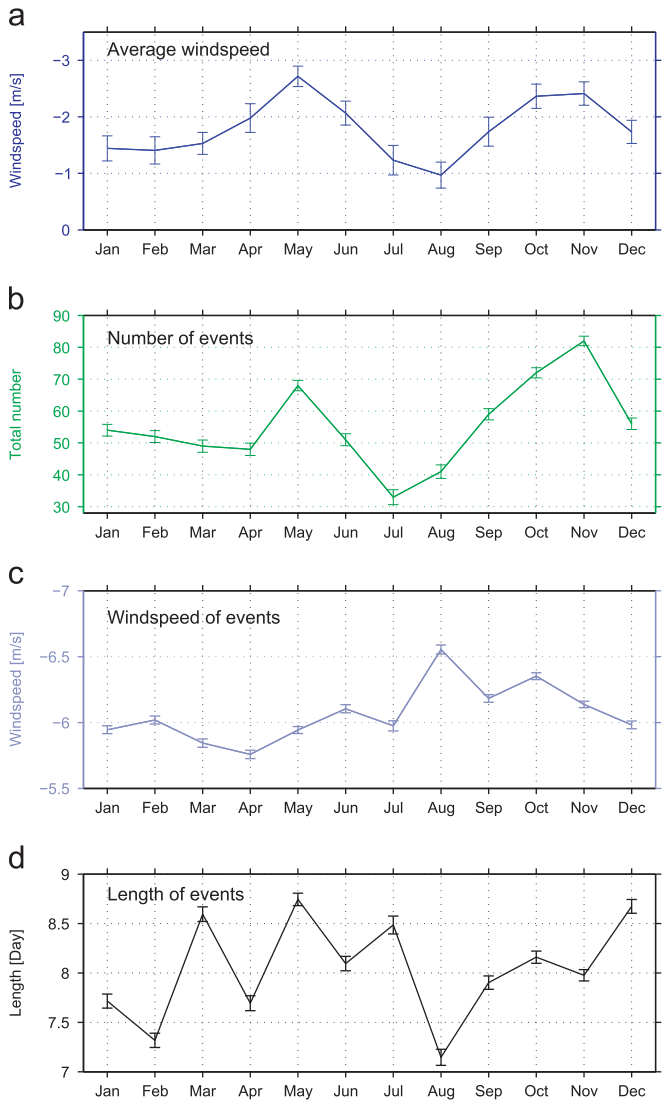

Fig. 4. (a) Climatological monthly mean wind speed along 105 °T for all 70 years, including the standard error. (b) Monthly distribution of the 665 upwelling events. (c) Climatological monthly mean wind speed of the upwelling events. (d) Climatological monthly mean length of the upwelling events.

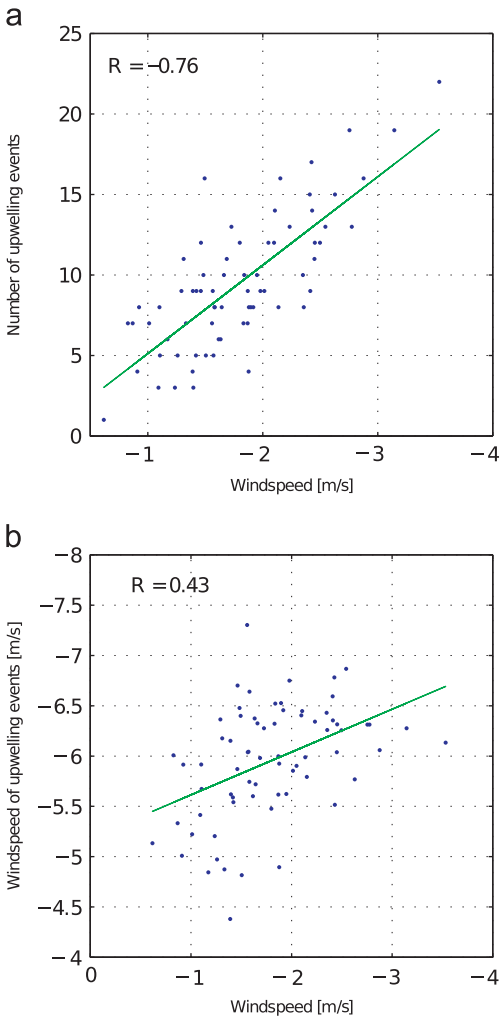

Fig. 5. (a) Regression of the annually-averaged wind speed along 105 °T and the number of upwelling events each year. (b) Regression of the annually-averaged wind speed along 105 °T and the average wind speed of the upwelling events each year.

period 1941–2010. This number increases to 1388 for weaker storms (exceeding 6 m/s and >4 days), which, according to Schulze and Pickart's (2012) relationship, should lead to 972 upwelling events. Hereafter, we assume that all of the 10 m/s storms caused upwelling, and we examine the characteristics and trends of these storms. We note that all but one of the storms matching this criterion during the two-year SBI mooring array period caused upwelling. It is important to remember, however, that this criterion likely misses many moderate-to-weak upwelling events along the Beaufort Slope. In fact, approximately half of the events measured by the SBI mooring array (22 out of 45) did not meet this criterion.

The number of strong upwelling events determined as such varies from year to year (Fig. 3b), with a maximum of 22 events in 2007 (which, notably, was the lowest ice-cover year in our time series), and a minimum of one event in 1954. The mean number of events is 9.5 ± 4.2 per year. It is clear that the number of strong upwelling events has increased over the last 25 years. During the decade of the 1970s the average number of events per year was 6, while during the most recent decade it was more than twice that. While there is a statistically significant correlation between yearly-mean wind speed and the number of upwelling events per year (Fig. 5a), the scatter is significant and hence it would be difficult to discern the number of upwelling storms in a given year based solely on the mean wind speed over that year.

Other metrics of interest are the strength and duration of the upwelling winds. Over the last 25 years, as the number of upwelling storms has increased, so has their average wind speed measured at Barrow (Fig. 3c). It is important to note that this does not imply that the storms as a whole are stronger, only that the associated wind speeds over the North Slope are enhanced. This is investigated further in Section 3.3. As was true for the number of events, the average strength of the events in a given year is statistically correlated with the overall average wind speed during that year (Fig. 5b). However, the scatter is pronounced, so again it would be hard to say anything precise about the magnitude of the upwelling events from the yearly-averaged wind data. Interestingly, there is little to no decadal variability in the length of the upwelling events (Fig. 3d). Using the long-term average storm length of 8 days together with the increased number of events in the latter part of the timeseries (Fig. 3b), this implies that, over the last two decades, the percentage of the year subject to upwelling has increased from 17% to 25%.

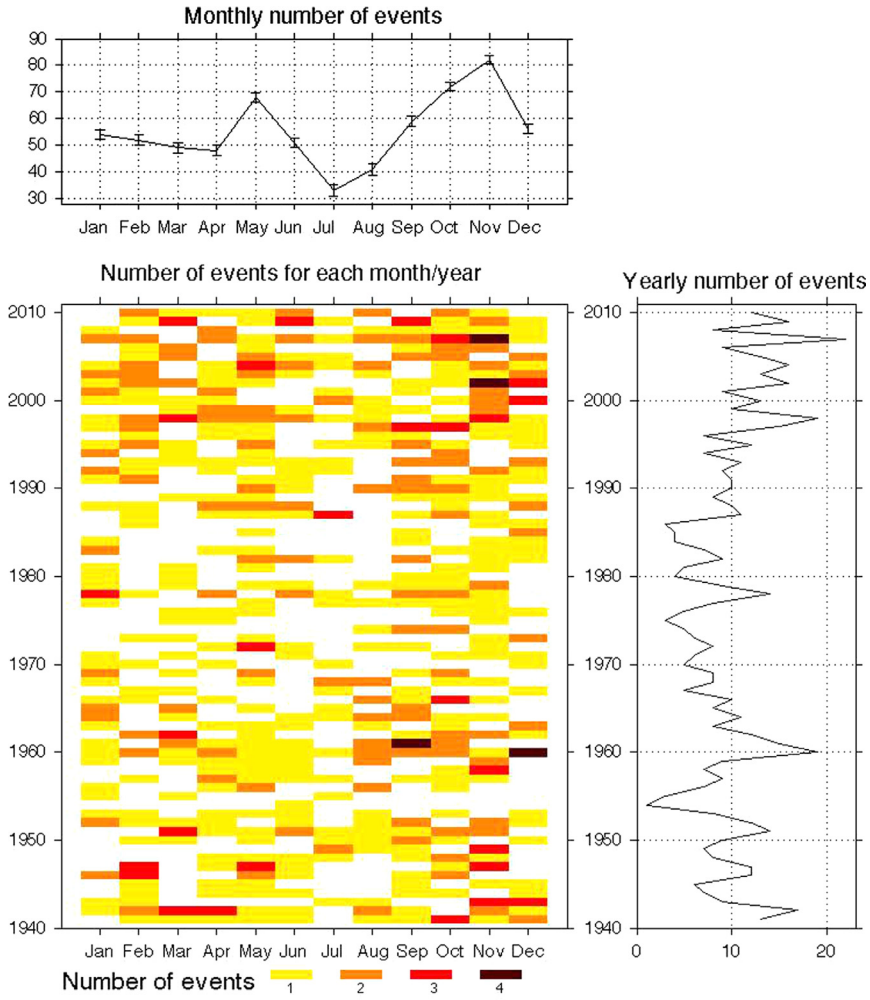

Fig. 6. Hovmoller plot (in color) of the number of upwelling events in each month and year. The white spaces correspond to periods without events. The top panel shows the total number of events for each month (sum of the columns, which is the same information as in Fig. 4b), and the right panel shows the total number of events for each year (sum of the rows, which is the same information as in Fig. 3b). (For interpretation of the references to color in this figure legend, the reader is referred to the web version of this article.)

The seasonality of the upwelling shows clear trends as well. In concert with the monthly-averaged winds, there are two peaks in the monthly number of strong storm events, one in May and the other in November. (Note, however, that the two peaks in upwelling frequency are more pronounced than in wind speed). November is the stormiest month, with a total of 82 events over the 70-year record (an average of more than one storm each year). July is the month that is most devoid of storms, with a total of 33 (an average of less than one storm every two years). A hovmoller plot of monthly storm counts (Fig. 6) provides an overview of the storminess of the North Slope region (see also Table 1). One sees that there are numerous periods over the 70-yr record when there was no monthly storm activity; in fact this is the most prominent occurrence in the hovmoller plot (43.6% of the time), followed by months with a single storm (38%). There were a few months when there were as many as four storms (0.5% of the time). These periods all occurred in the fall (keep in mind that we are tabulating only strong events and their average duration is 8 days, hence four events in a month means that the entire month was subject to upwelling). We note that 1954 had the most storm-free months (11), while July had the most storm-free years (43 out of 70). Conversely, 1947 and 2009 had the most months with 3+ storms (3), and November had the most years with 3+ storms (7).

Perhaps surprisingly, the seasonality in the strength of the upwelling events is unrelated to the storm frequency (Fig. 4c). Although there are more storms in May and November, there is nothing special about the strength of the storms during these two months. Curiously, the strongest storms occur in August. Hence, although there are relatively few storms that month, when they do occur they are powerful. We note also that even though November has more numerous and stronger storms than May, the monthly averaged wind speed is higher in May (Fig. 4a). This suggests that the background winds in May are stronger. To test this we computed the easterly winds during each of the months in the absence of high wind speed events, and this revealed that the winds are indeed more consistently out of the east during May. The different nature of the upwelling in May versus November is explored further in Section 3.3. Finally, there are no compelling seasonal trends in the length of the upwelling events (Fig. 4d). However it is of interest to note that while the strongest upwelling

Table 1
Number of months during the time period 1941–2010 (total of 840 months) associated with the given number of strong storms, including the percentage.

Number of storms	Total number of months	Percentage
0	366	43.6
1	319	38
2	123	14.6
3	28	3.3
4	4	0.5

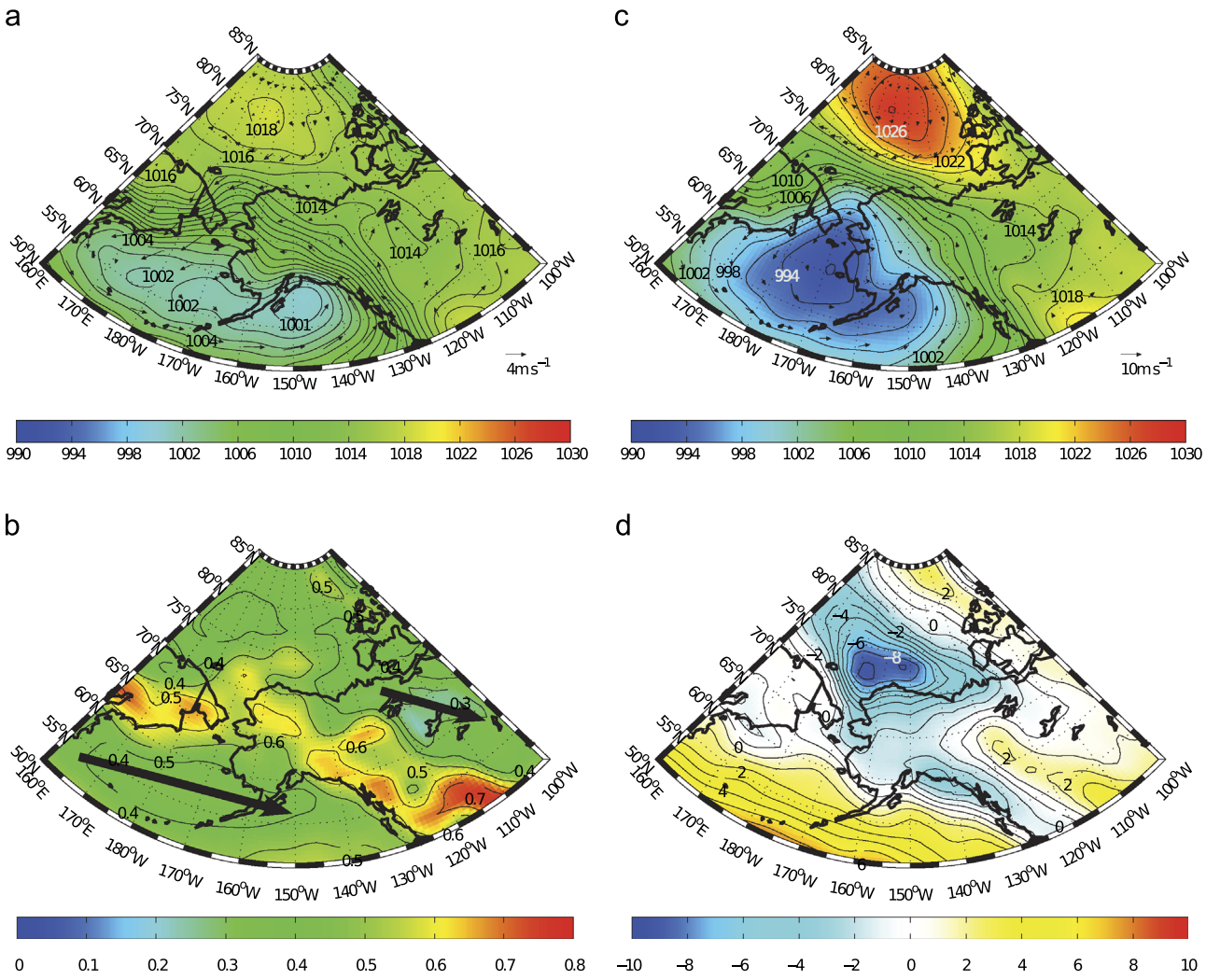

Fig. 7. Synoptic atmospheric circulation during the month of November for the NCEP time period (1948–present). (a) Monthly mean sea-level pressure (contours and shading, mb) and 10 m wind (vectors, m/s). (b) Monthly mean directional constancy of the 10 m wind with the average storm track indicated. (c) Composite of the sea-level pressure (contours and shading, mb) and 10 m wind (vectors, m/s) during upwelling events. (d) Composite of the zonal component of the 10 m wind (m/s) during upwelling events.

events occur in August, these storms are not only infrequent, but on average they are the shortest in duration.

3.2. Relationship of upwelling to climate indices

One wonders if the interannual to decadal variability present in the upwelling metrics is related to any of the known long-term climate trends and atmospheric indices. To address this we first examine the low-frequency content in the upwelling timeseries using Singular Spectrum Analysis (SSA). This is a non-parametric analysis technique that uses data-adaptive functions to separate a time series into components that are statistically independent and that maximize the variability in the original time series (see Ghil et al., 2002). This approach has an advantage over other spectral techniques, such as Fourier Transforms, in that it allows for more complex temporal variability that is not described by trigonometric functions. Applying the SSA technique to our timeseries of upwelling metrics, we identified statistically significant variability with a time-scale on the order of 40 years in both the number of upwelling events per year and the strength of the upwelling events. This variability may be related to the Low Frequency Oscillation (LFO) identified by Polyakov et al. (2003) in maritime Arctic surface air temperature and sea-level pressure data. The LFO is characterized by two periods of warming, one in the 1930–1940s and the other in more recent decades. Interestingly, our results indicate an increased occurrence of upwelling events and stronger events during these two periods (Fig. 3b and c, although the decade of the 1930s was excluded from our analysis due to concerns about data coverage and integrity, see Section 2.2).

Next we determine if the observed long-term trends in upwelling are related to any of the atmospheric patterns such as the Arctic Oscillation (AO), the Dipole Anomaly (DA), or the North Pacific Index (NPI). The AO is the dominant interannual mode of atmospheric circulation in the Arctic domain (Thompson and Wallace, 1998), which has been shown to be related to the cyclonic versus anti-cyclonic regimes of ocean circulation in the western Arctic (Proshutinsky and Johnson, 1997). The DA is the second atmospheric mode, which is argued to be more pertinent in influencing the Arctic-wide patterns of ice distribution (Wang et al., 2009). The NPI is defined as the area-weighted sea level pressure over the Bering Sea and a portion of the North Pacific Ocean (Trenberth and Hurrell, 1994). The NPI is related to the strength of the Aleutian low, and has been shown to be linked to storm track behavior in the North Pacific (Rodionov et al., 2005).

We regressed our upwelling metrics against these three atmospheric indices. For the first two (the AO and DA) we found no

statistical correlation with the number of upwelling events or the strength of the events. This was true whether we used winter averages or monthly values of the indices. In fact, there was no significant relationship between the average wind speed measured at Barrow (i.e. irrespective of upwelling or not) and either of these atmospheric modes. On the other hand, the wind speed at Barrow was significantly correlated with the NPI index during the winter season, such that lower values of the index correspond to stronger easterly winds. In light of the results of Pickart et al. (2009a) this is perhaps not surprising, since Aleutian low pressure systems can be broad enough to influence the southern Beaufort Sea. However, the two upwelling metrics (number of events and strength of events) are not significantly correlated with the NPI. This is likely because both the precise nature of the storm tracks as well as the Beaufort High play a role in driving the upwelling, as investigated next.

3.3. Broad-scale atmospheric context

It is of interest to consider the large-scale atmospheric patterns that result in upwelling along the Beaufort slope, which shed light on both the seasonality of the upwelling as well as the interannual trends described above. Pickart et al. (2009a) conducted a detailed study of storm patterns and their relationship to upwelling for a single season (autumn 2002). They found that, while upwelling events were caused by low pressure systems passing near the Aleutian island arc and Alaskan Peninsula, not all such Aleutian lows triggered an event. Rather, it was mainly those storms with northward-directed trajectories. Furthermore, they found that upper-level atmospheric blocking patterns in late-fall/early-winter prohibited some of the storms from triggering upwelling along the North Slope. Here we focus on three particular months: November, May, and August. As seen above, the first two months have the highest frequency of upwelling events. We include August as well because that month is within the open water season and hence is pertinent to the biological analysis in Section 4. Among other things, we seek to clarify the role of the two centers of action – the Aleutian low (AL) and Beaufort High (BH) – in contributing to the upwelling.

The summer atmospheric circulation over the western Arctic Ocean is dominated by the anti-cyclonic flow of the BH (Reed and Kunkel, 1960; Walsh, 1978). At other times of the year, it exists as an extended ridge of high pressure emanating northeastward from the Siberian High (Walsh, 1978). The AL represents the integrated impact of low pressure systems that transit the North Pacific from the northeast coast of Asia towards the Gulf of Alaska region (Wilson and Overland, 1986; Pickart et al. 2009b). The AL exhibits considerable seasonal variability. It is most intense during the winter months (Mesquita et al. 2010), while during the summer it weakens and moves northwards as a region of high pressure is established in the Northeast Pacific.

Using the NCEP data we constructed climatological monthly composites as well as composites for the periods of the month

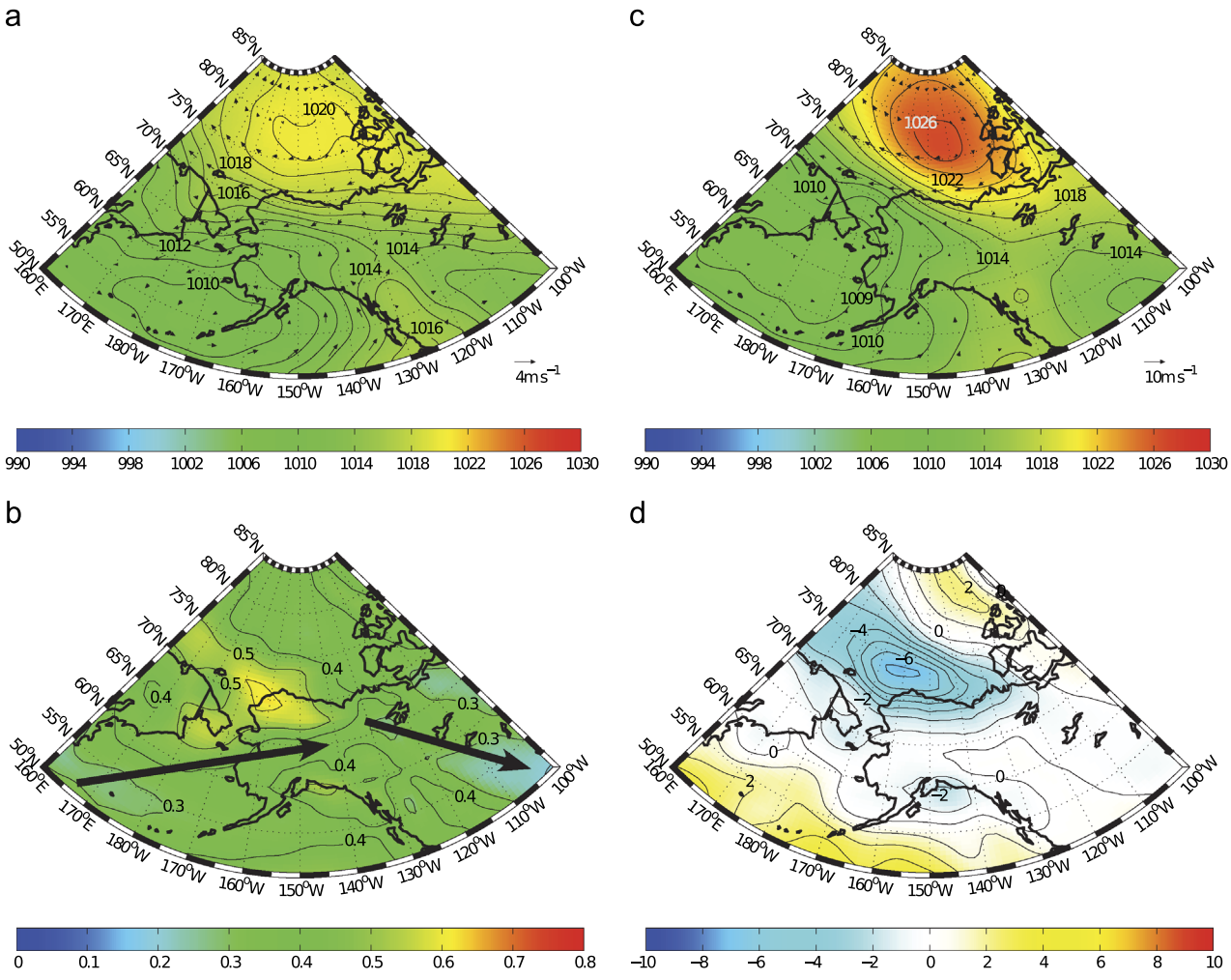

Fig. 8. Same as Fig. 7 for the month of May.

when strong upwelling was occurring according to the Barrow timeseries. Since the storm season is in the fall, and Pickart et al. (2009a) focused on the fall as well, we begin with the month of November (Fig. 7). One sees that both the AL and BH are evident in the monthly composite (Fig. 7a). A useful metric for determining the location of the storm track is the directional constancy (Moore, 2003). A low value of directional constancy is indicative of variable wind direction, which is the case for propagating storms. Not surprisingly, there is a minimum in directional constancy in the vicinity of the Aleutian Island chain and Alaskan peninsula during the month of November (Fig. 7b). This is consistent with the storm track analysis of Pickart et al. (2009a) for autumn 2002. During upwelling events one sees a striking change in the two centers of action (Fig. 7c): the AL deepens markedly and the BH intensifies. This indicates that both centers of action contribute to the upwelling; in particular, it is the strengthened gradient in sea level pressure (SLP) that causes the enhanced easterly winds. The 10 m wind speed composite (Fig. 7d) indicates easterly winds near 10 m/s during upwelling along the North Slope.

The November composites are perhaps not surprising in light of the results of Pickart et al. (2009a) and given the fact that November is the heart of the storm season (Mesquita et al. 2010). However, it should be emphasized that Pickart et al. (2009a) only investigated a single autumn versus the 70-year period considered here. In contrast, the reason for the enhanced frequency of upwelling in May is not at all obvious since the AL is significantly weaker during that time of year. The monthly SLP composite for May again shows the signature of the two centers of action, but the upwelling SLP composite is markedly different in May versus November (compare Figs. 7c and 8c). In particular, the strength of the BH is the same, but the AL is not nearly as deep. The key to the upwelling in May can be seen in the directional constancy composite which indicates that the storm track at this time of year is situated farther to the north (Fig. 8b). The implication is that, while there are overall fewer Aleutian lows in May than November, a greater percentage of them cause upwelling because of their closer proximity to the North Slope. It is also important that the BH is strong, which contributes to the SLP gradient in the region of upwelling. Again one sees enhanced easterly wind speeds, though not as strong as in November, consistent with the Barrow timeseries (Fig. 4c).

Unlike November and May, August does not stand out in terms of the number of storm events (only July has less-frequent upwelling, Fig. 4b). However, recall that when upwelling does occur in August the winds are stronger than in any other month (Fig. 4c), although the events last the shortest (Fig. 4d). The monthly composite for August (Fig. 9) barely shows any signature of the AL, and only a weak signature of the BH. During the periods of upwelling, however, both centers of action are enhanced. Interestingly, during these periods the BH is weaker than the other two months, but the AL is stronger than in May. Furthermore, the storm track in August is farther north than in May. It is

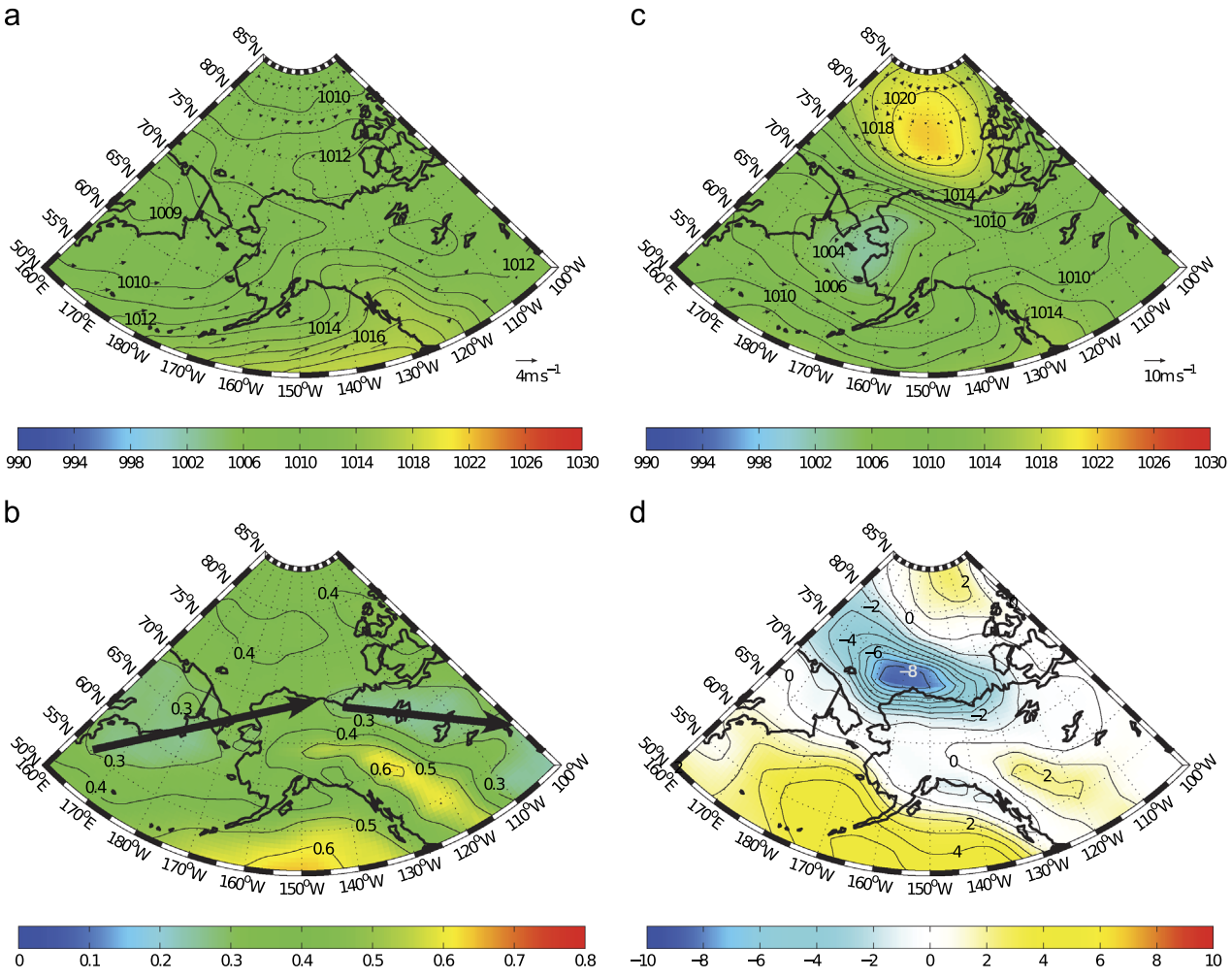

Fig. 9. Same as Fig. 7 for the month of August.

due to this combination of extreme northerly storm track plus moderately deep AL (and moderately high BH) that causes the strong August winds (Fig. 9d).

Finally, we computed leading/lagged composites of the storm events using the NCEP data, which provide a sense of the time evolution of the upwelling SLP composites presented in Figs. 8–10. We found that the BH is remarkably stationary over the duration of an upwelling event in each of the months. By contrast, there is some indication of propagation of the AL during storm events in May and August, and strong evidence of such propagation during November events. Hence, one could argue that the stationarity of the BH provides much of the background support for the generally easterly flow along the North Slope, and the transient appearance of the AL provides additional support for the enhanced winds that drive upwelling.

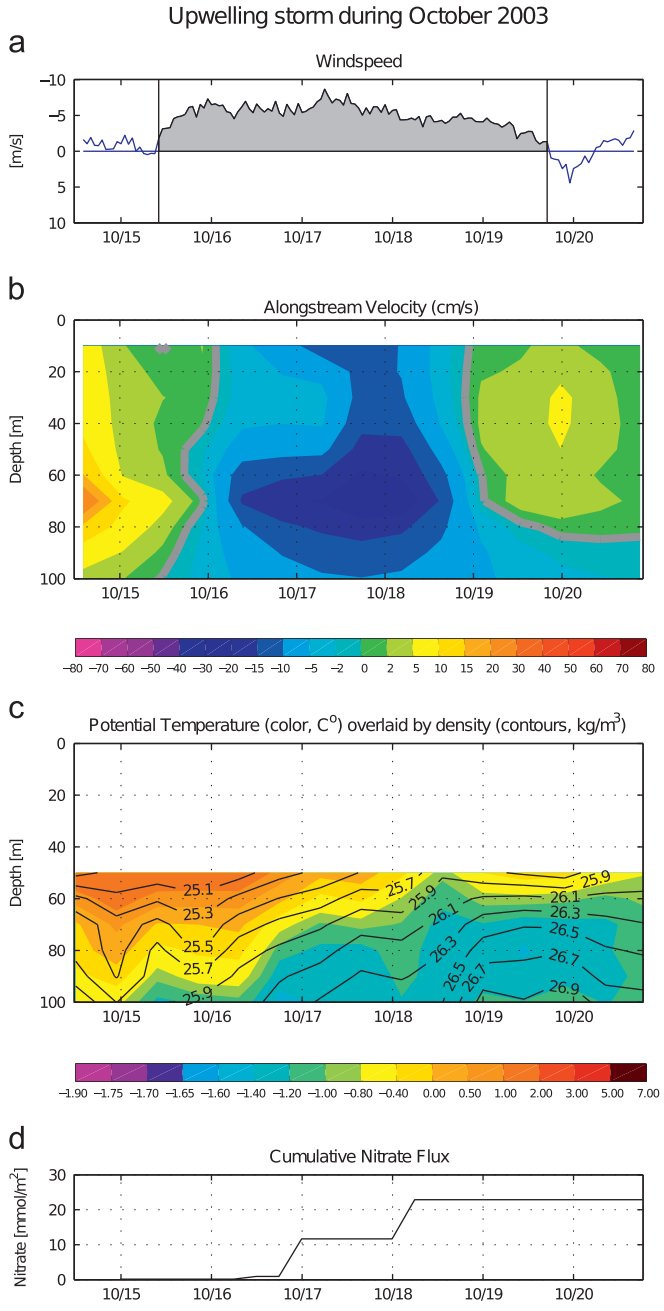

Fig. 10. Upwelling characteristics for a storm in October 2003 at a cross-slope distance of 16 km. (a) Wind speed along 105 °T measured at the Barrow meteorological station. The grey shaded area indicates the length of the storm. (b) Alongstream velocity (cm/s) of the water column during the event (see Schulze and Pickart (2012) for more details). Positive flow is to the east and negative flow to the west. (c) Potential temperature (color, °C) overlain by potential density (contours, kg/m^3). (d) Cumulative Nitrate flux in mmol/m^2 (see text for details).

4. Biological implications of upwelling

4.1. Upwelling-induced nitrate fluxes

The presence of Pacific Winter Water on the Chukchi shelf, with its high concentration of nutrients, triggers a phytoplankton bloom every year as the ice retreats and the sunlight becomes more intense. Based on in-situ measurements (Hill and Cota, 2005) and satellite ocean color data (Pabi et al., 2008), the bloom has typically peaked by mid-August. At this time the nutrients in the surface layer are largely stripped and the supply of winter water on the shelf has all but disappeared. However, the common occurrence of upwelling provides a mechanism of bringing the nutrient-rich winter remnant water, which resides just offshore of the shelfbreak in the halocline, upwards into the euphotic zone—possibly spurring additional primary production late in the season. As shown above, upwelling increases significantly from September into October, and since the freeze-up is occurring later in the year (Markus et al., 2009), this could result in favorable conditions for the onset of a fall bloom. In addition, although summer storms are more rare, our wind analysis demonstrates that August events are in fact the strongest. This suggests that wind-induced productivity could also occur in summer.

In order to estimate the wind-driven delivery of nitrate into the upper layer, we calculated vertical nitrate fluxes for the seven upwelling events that occurred from August to early-October during the two-year SBI mooring array deployment period (see Table 2 for the list of storms and their characteristics). As discussed in Schulze and Pickart (2012) this is the open-water upwelling season. We note that only three of these storms qualified as strong upwelling events according to the criterion used in the previous section, and none of them were particularly strong (all were below average in wind strength). During this time of year, warm low-nutrient Alaskan Coastal Water in the upper layer generally lies above the colder, nitrate-rich Pacific winter remnant water in the upper halocline (von Appen and Pickart, 2012). During upwelling the colder high-nitrate water replaces the warm upper layer water.

The evolution of an upwelling event is nicely illustrated by constructing a time-depth plot at a given cross-stream location (Fig. 10). (Features are similar for other locations across the slope.) One sees the westward reversal of the shelfbreak jet in response to the wind and the upward displacement of the density surfaces. For the storm in question, isopycnals as dense as 25.7 kg/m^3 (the upper part of the winter remnant water) entered the layer above 50 m. Note that the isopycnals did not immediately relax once the winds subsided and the shelfbreak jet began to re-establish itself

Table 2
The seven storms identified during the open water period of 2002–2004, when the SBI mooring array was deployed, and their characteristics.

Date	Length [days]	Max wind (easterly) [m/s]	Average wind [m/s]
12 Sep 2002	6.6	8.8	4.47
10 Oct 2002	2.5	11.1	6.84
13 Aug 2003	4.2	12.5	7.6
06 Oct 2003	2.7	13.8	10.09
10 Oct 2003	1.7	9.9	5.23
15 Oct 2003	4.8	8.6	5.03
22 Aug 2004	4.1	10.6	5.55

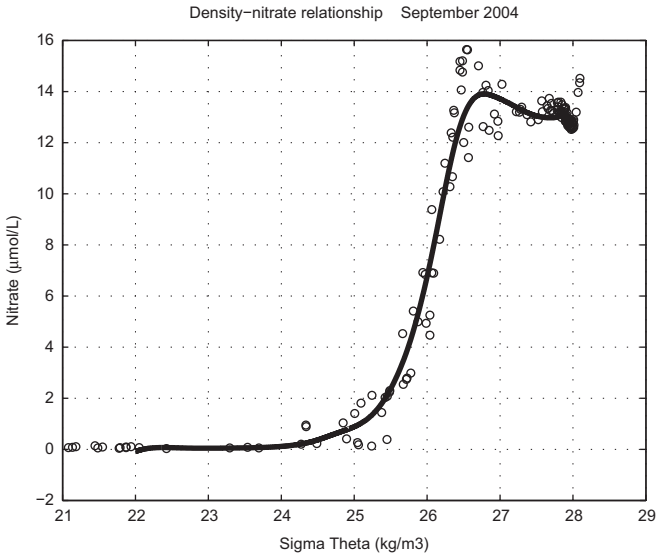

Fig. 11. Density–Nitrate relationship determined from the in-situ data in September 2004 at the mooring site. The solid curve is a low-pass of the individual points.

to the east, which is typical of these events (see also Pickart et al., 2011).

To compute the nitrate flux for the storms we first established a density–nitrate relationship. This was done using the shipboard CTD and water sample data obtained near the array in September 2004 (Fig. 11). The scatter of points revealed a well-defined relationship where the upper ~25 m was stripped of nitrate, and the concentration increased sharply through the halocline to values in the range of 14 μmol/L in the Pacific winter remnant water. It is likely that the shallow waters of the Beaufort Sea were similarly stripped of nitrate starting in August. A low-passed curve was fit to the scatter in Fig. 11.

The nitrate flux calculation was carried out using the timeseries of vertical sections of potential density. In particular, we tracked the displacement of isopycnals in the water column during upwelling events. Using this information, we computed the upward vertical velocities at 50 m (i.e. the upper boundary of the vertical sections) for each 2 km grid point across the section with a time resolution of 6 h. Applying the (low-passed) density–nitrate relationship we then determined the cumulative flux of nitrate into the upper 50 m for each of the seven events. We note that even though the array spanned a cross-shelf distance of 40 km, the data coverage in the upper 100 m at the outer three mooring sites was somewhat sparse for three of the seven storms. Consequently we limited the calculation to the upper-slope (cross-stream distance of 24 km). This does not imply, however, that upwelling did not take place farther offshore. In fact, the storms with complete data coverage at the outer moorings did result in a nitrate flux into the upper 50 m over the mid-slope.

Since the nutrient concentrations within the upper layer are depleted in late-summer/early-fall, upwelling has the potential to drive new production at levels not typically observed at this time of year. The 2002–2004 SBI mooring array sampled all or part of three open water seasons. Our results indicate that for the three seasons in question, the storm events supplied between 36 and 326 mmol N/m^2, with an average of 142 mmol N/m^2 per season and 61 mmol N/m^2 per storm (Table 3). (Keep in mind that only three of the storms in question are considered strong.) How does this wind-driven supply of nutrients compare to the quiescent background state? During non-upwelling periods, stratification limits "new" sources of nitrogen mainly to that associated with diffusion from below. Unfortunately no estimates of diffusivity

Table 3
Nitrate flux and carbon uptake during the open water season from 2002 to 2004, based on the seven storms listed in Table 2. Included is the annual average and per storm average.

Season	N Flux [mmol/m^2]	C uptake [mmol/m^2]
2002	63	418
2003	326	2150
2004	36	239
Annual open Water average	142	936
Per storm average	61	401

exist for our study region. However, using autumn microstructure measurements together with nitrate data in Amundsen Gulf in the Canadian Beaufort, Bourgault et al. (2011) estimated diffusivities and turbulent nitrate fluxes. They computed a mean upward flux of nitrate between 0.3 and 0.8 mmol N/m^2, which is considerably smaller than the average N flux computed here due to storm-induced upwelling during the open water season (Table 3).

4.2. Dynamical context for the upwelling

The wind-driven nitrate flux calculated above was an empirical estimate using the mooring and shipboard data. Using simple dynamics we can check the consistency of this value via a scale analysis. As discussed in Janowitz and Pietrafesa (1980), upwelling is enhanced in the vicinity of the shelfbreak due to the increase in bottom slope there and the fact that the water column is relatively shallow (versus the deep slope). Based solely on kinematics, the vertical velocity at the bottom during an upwelling event is $w=h_y v$, where v is the onshore velocity and h_y is the bottom slope in the cross-stream direction y. As demonstrated in Schulze and Pickart (2012), the onshore transport during upwelling events approximately balances the offshore Ekman transport near the shelf edge in this part of the Beaufort Sea. Schulze and Pickart (2012) found that the mean shelf-basin exchange rate for a storm is 1.3 Sv, and the mean Ekman depth is 45 m. Note that this is the depth of the mooring top floats, and hence approximately the depth at which we calculated the vertical velocities above.

Assuming that w vanishes at the sea surface and that it has a linear profile versus depth, we can use the above relationships to estimate a scale for the vertical velocity that pumps fluid into the upper layer, $W \sim \alpha V(h_{ek}/H)$, where α is the average bottom slope in the vicinity of moorings BS2 and BS3 (.0135), V is the average onshore velocity in the lower layer, h_{ek} is the Ekman depth (45 m), and H is the average water depth between BS2 and BS3 (115 m). The mean storm exchange rate of 1.3 Sv translates into a cross stream velocity of 6 cm/s (where the alongstream length scale of the upwelling is 500 km, see Schulze and Pickart, 2012). For the specific open water storms considered in this study, the average onshore velocity is 4.5 cm/s. Using the latter value, the scale for the vertical velocity is $W \sim 20$ m/day.

How does this value compare to our empirical estimate? For the six storms in question we computed the average time over which the nitrate was delivered to the upper layer, the average vertical velocity over this time interval at the top boundary of our vertical sections (the base of the Ekman layer), and the average nitrate concentration at this depth during the event. The product of these three quantities is 60 mmol N/m^2. This is the nitrate flux for the "average storm", which turns out to be virtually identical to the mean of the nitrate fluxes for each of the individual storms presented above (61 mmol N/m^2, Table 3). Thus, our average storm considered in this fashion should provide a meaningful estimate of the average vertical velocity. The value we obtain is 15 m/day, which is very much in line with our scale estimate (20 m/day). This gives us confidence that our empirically derived nitrate fluxes

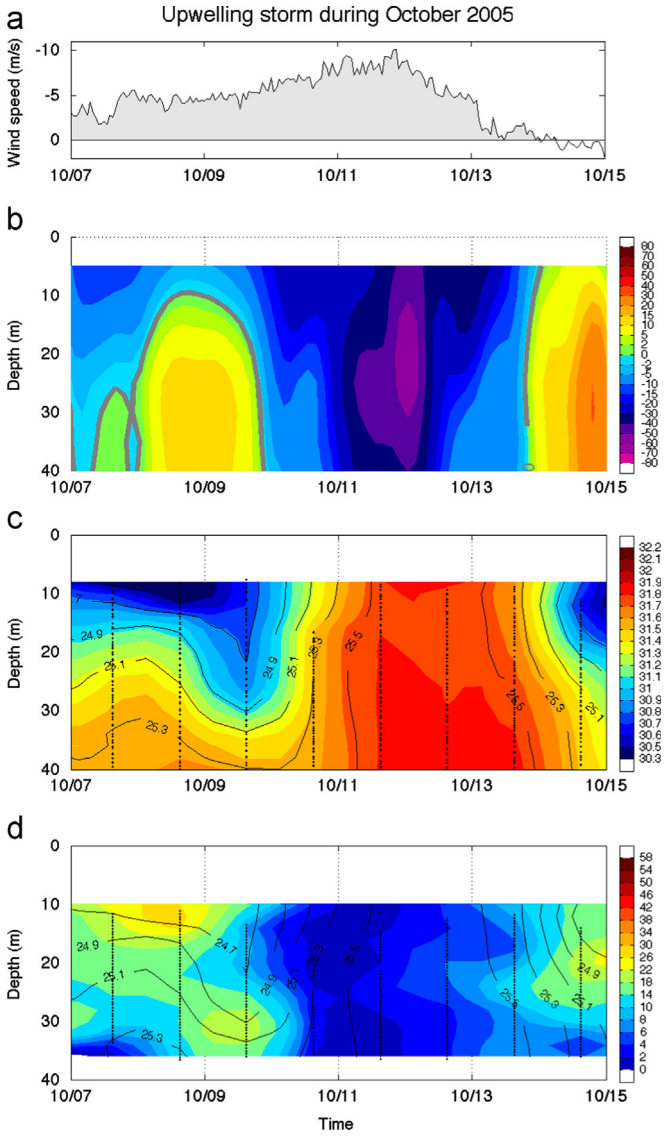

Fig. 12. Upwelling characteristics in the upper part of the water column for a storm in October 2005 at the BS3 mooring site (cross slope distance of 20 km). (a) Wind speed along 105 °T measured at the Barrow meteorological station. (b) Alongstream velocity (cm/s) of the water column during the event. Positive flow is to the east and negative flow to the west. (c) Salinity (color) overlain by potential density (contours, kg/m^3). (d) Buoyancy frequency (color, $1/s \times 10^{-3}$) overlain by potential density (contours, kg/m^3). The black dots in (c) and (d) mark the data points of the coastal winched profiler.

are reasonable. Next we assess the impact of this flux on primary productivity.

4.3. Estimate of primary productivity

Previous work in the Canadian Beaufort Sea, to the east of our study area, has demonstrated that phytoplankton growth occurs in response to upwelling favorable winds. Using in-situ measurements in the vicinity of Cape Bathurst in October 2007, Tremblay et al. (2011) documented new production associated with high-salinity upwelled waters (before the onset of the seasonal ice pack). In the absence of comparable field data in our region, we assume that all of the nitrate transported into the upper 50 m is available for primary production. As such, this represents an upper bound. However, as noted above, the relaxation phase of the storms (i.e. the subsequent deepening of the isopycnals) tends to last significantly longer than the spin-up phase. For the storm presented in Fig. 10 the isopycnals remained elevated for more than four days, which is enough time to initiate phytoplankton growth. The average duration of strong wind events in the 70-year timeseries is 8 days. Furthermore, it is likely that enhanced wind-induced turbulent mixing during the storms will cause some of the nitrate to remain in the upper layer even after the isopycnals relax. During late-summer the Beaufort shelf/slope receives 18–22 h of sunlight per day, decreasing to 9–13 h during the early-fall. There is little to no ice during this season, and the 1% light layer extends to 30 m (Grebmeier, pers. comm., 2012). Therefore, even though our nutrient flux calculation represents an upper bound, it is not unreasonable to assume that a good fraction of the upwelled nitrate reaches the euphotic zone and is utilized by primary producers.

Given these assumptions and conditions, if all of the nitrate supplied by storms is converted into phytoplankton biomass (C:N=6.6), the estimated C uptake for the three years ranges between 239 and 2150 mmol C/m^2 per season, with an average of 936 mmol C/m^2 per season and 401 mmol C/m^2 per storm (Table 3). These values can be put into perspective using in-situ data collected during the SBI program. During the August 2002 SBI process cruise, ^{14}C primary productivity measurements were made over the shelf and slope of the Chukchi and Beaufort Seas (Hill and Cota, 2005). The average Hill and Cota (2005) primary productivity estimates for stations in a comparable depth range to our study domain were 29.8 and 68.4 mmol C/m^2/d for the Beaufort and Chukchi Seas, respectively. If we assume that these daily estimates were constant over a 60 day growing season, our seasonal average of wind-driven production for the Beaufort slope is only a factor of 2–4 lower than their C uptake rates (1790–4110 mmol C/m^2 per season). We note that there were no storm events during July/August 2002, the time of the Hill and Cota study. Hence, carbon fixation from short-lived, episodic wind events as reported here could be on par with carbon fixed during the summer growing season in the absence of storms. It should be pointed out that we are expressing carbon fixation as a unit area flux (mmol C/m^2); however, the Chukchi shelf/slope is roughly four times larger than the Beaufort slope. This implies that the total integrated carbon production will be larger in the Chukchi Sea (although the satellite analysis of Arrigo et al. (2008) implies that carbon fixation could be comparable in the two seas).

4.4. Mixed-layer considerations

Because the CTD profilers on the moorings did not extend into the upper layer, we are unable to quantify the fate of the upwelled nutrients during the storms, and, consequently, could only present upper bounds on the potential primary productivity. However, during the year following the SBI program a single mooring was deployed in the core of the shelfbreak jet, at the same location as BS3, which collected hydrographic data in the upper part of the water column. This allows us to demonstrate that late-summer/early-autumn upwelling storms can result in deep mixed-layers that should permit the nutrients to penetrate the euphotic zone.

The BS3 mooring deployed in 2005–2006 contained a tandem of moored profilers. The lower profiler was the same as that used during the SBI program and extended from near the seafloor to 45 m depth. The mooring's top float, situated at 40 m, contained a device known as a coastal winched profiler. This consists of a CTD on a small buoyant sphere connected via a nylon line to a winch on the top float. Once per day the buoyant float would release and rise to 10 m depth, or the underside of the pack ice, then get pulled back down to the top float and transfer its data to a logger. This provided a timeseries of hydrographic vertical profiles of the upper part of the water column at 2 m resolution for the entire year.

Between August–October, 2005 there were six upwelling events, one of which is shown in Fig. 12. One sees that, like the event shown in Fig. 10, the shelfbreak jet reverses to the west in response to the easterly winds (Fig. 12a and b). However, it is now clear that the upwelling extended to less than 10 m depth, clearly into the euphotic zone. It is also evident that the mixed-layer during this storm extended to greater than 40 m—as indicated by the near-vertical isopycnals and the associated small values of the buoyancy frequency (Fig. 12c and d). This is consistent with the typical Ekman depth of 45 m documented in Schulze and Pickart (2012). Although the stratification remains non-zero in Fig. 12d at the height of the upwelling, this should still be considered a mixed-layer. Such weakly stratified mixed-layers are common in other oceanographic settings, such as the bottom layer of shelfbreak jets (Pickart, 2000) and the surface layer during active wintertime convection (Pickart et al., 2002).

Note in Fig. 12c that the 25.5 kg/m^3 isopycnal extends shallower than 10 m and likely outcrops. This was one of the last isopycnals to "disappear" during the storm presented in Fig. 10, and suggests that after it was no longer sampled by the moored profiler it encountered the mixed-layer and fluxed nitrate close to the surface. We stress, however, that the evidence presented in Fig. 12 does not imply that all upwelling storms extend this shallow in the water column. Of the six open water storms measured by the winched profiler in 2005, four had near-zero stratification (i.e. mixed-layers extending to at least 40 m as in Fig. 12), one was weakly-stratified, and one remained significantly stratified in the upper layer. The latter two, however, were the weakest storms. The important point here is that the late-summer/early-fall upwelling described in this study can, on occasion, supply nutrients to the euphotic zone. It is likely that much of the resulting carbon production will be subsurface, contributing to a deep chlorophyll maximum. However, as presented next, surface blooms may also occur via this process.

4.5. Satellite evidence of a storm-induced bloom

Because of the sporadic and unpredictable nature of upwelling events, it is very difficult to obtain in-situ primary productivity measurements in the aftermath of a storm to demonstrate the existence of wind-induced blooms. While Tremblay et al. (2011) documented such enhanced production following upwelling in the Canadian Beaufort Sea, we are unaware of comparable water column measurements in the Alaskan Beaufort Sea. Consequently, we turned to satellite ocean color data which is available from 1998 to present. Not surprisingly, however, clouds nearly always obscure the images during stormy conditions. Furthermore, bottom sediments resuspended by the storms could dominate the satellite signal. Even though open water persists well into October in the southern Beaufort Sea, there are no valid ocean color data after roughly the third week of September. This removes from consideration a substantial part of the season. Using the upwelling dates from the Barrow wind record for the period of the satellite data, we found only one event, from 5 to 13 August, 2010, where there were enough cloud-free pixels to discern whether or not there was a sea surface response in ocean color due to upwelling. We offer this as anecdotal evidence that storm-induced surface blooms do occur.

Fig. 13 shows the MODIS/Aqua chlorophyll *a* concentrations along the North Slope of Alaska prior to the storm event (August 4) and near the tail-end of the event (August 12). The location of the mooring array is marked in the figure, and Pt. Barrow is the northern-most extent of land. We applied a turbidity mask to the images (shown in pink on the right-hand panels) in order to isolate the biological signal. One sees that before the storm (top row) there is enhanced ocean color along the inner Beaufort shelf, as well as a tongue emanating from Barrow Canyon. Note, however, that this entire signal is due to high turbidity. Under weak wind forcing (which was the case at the time of the image) the

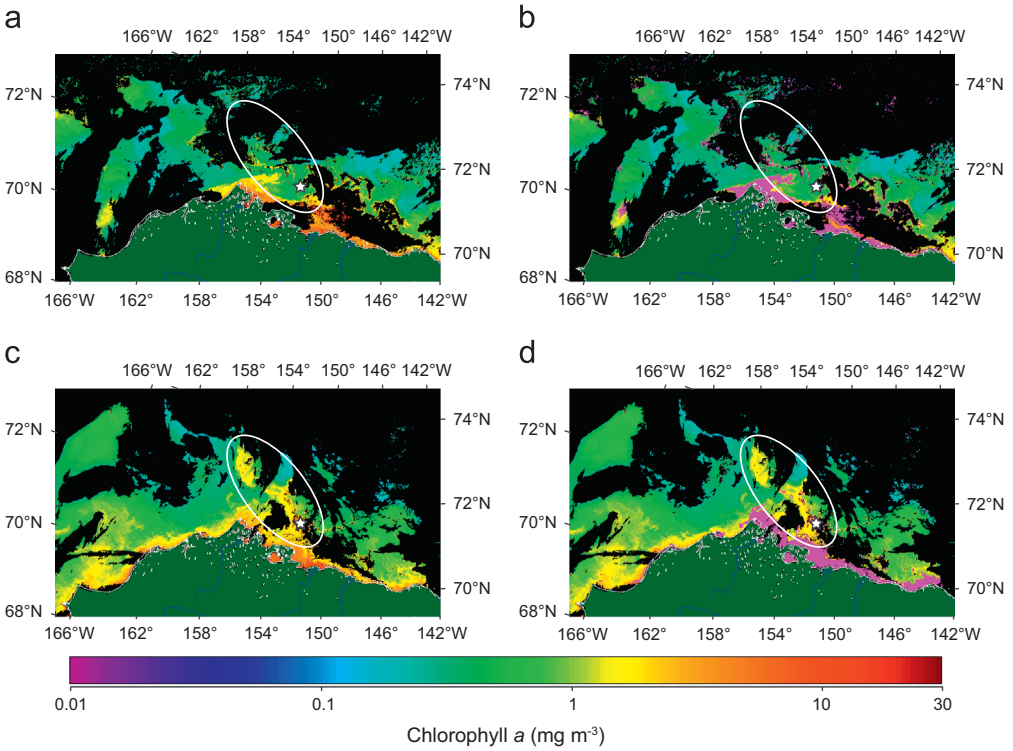

Fig. 13. Ocean color image of the study area, where color indicates the amount of chlorophyll. The location of the mooring array is denoted by the white star. (a) Productivity two days before the wind event in August 2010 (4–5 August). (b) Same as (a) but with turbidity flags (pink). (c) Chlorophyll 4 days after the wind event (14–17 August). The white ellipse shows the area of high productivity near the mooring array. (d) Same as (c) but with turbidity flags. (For interpretation of the references to color in this figure legend, the reader is referred to the web version of this article.)

normal summertime flow pattern consists of the Alaskan Coastal Current streaming out of Barrow Canyon and turning to the east along the Beaufort shelf and shelfbreak (Okkonen et al., 2009; von Appen and Pickart, 2012). This current carries low nutrient water that is not expected to support biological production. However, sediments from the head of the canyon are likely to be advected by the flow. This explains the tongue of high turbidity emanating from Barrow Canyon seen in the image prior to the storm.

After the storm there is a clear ocean color signal in the vicinity of the mooring array, extending northwestwards along the edge of the Chukchi Sea. Chlorophyll *a* concentrations have increased approximately five-fold in these waters (delineated by the circle in Fig. 13), which is assumed to be in response to the upwelled nutrients during the 8-day storm. As discussed earlier, the circulation during these storms is dominated by a westward-flowing jet, some of which will likely flow up Barrow Canyon (Pickart and Fratantoni, 2011) and some of which may either "jump" the mouth of the canyon or flow around the mouth and progress along the continental slope of the Chukchi Sea. Presently, the broad circulation response to easterly wind forcing in this region is not well understood, but the model results of Pickart et al. (2013) suggest that upwelled waters progress much farther to the west than they do offshore during such storms. This is consistent with the post-storm image of Fig. 13, adding credence to our assertion that the image shows evidence of a storm-induced bloom. We note also that Tremblay et al. (2011) documented enhanced satellite-derived productivity following upwelling in the Canadian Beaufort Sea.

4.6. Long-term trends

Using the upwelling metrics derived from the Barrow wind data, we can extend our results to assess the storm-induced primary productivity over the 70-year record. To do this we computed the carbon uptake rate for the storm with the largest nitrate flux during the SBI open water period (the reason being that the storms identified in the Barrow wind record were the strongest events). This resulted in a C uptake rate of 314 mmol/m^2/d. Note that this only applies for the time over which the isopycnals were rising during the storm, not the full length of the storm. In all of the events measured during SBI, the nitrate flux ceased before the winds diminished. This is not to say that the isopycnals relaxed – they remain elevated even after the storms are over – but the vertical velocity goes to zero before the winds subside. On average, for the 7 open water storms during SBI, the upward nitrate flux lasted for 60% of the storm.

Applying this percentage to each of the storms identified in the Barrow wind record between mid-August and late-October, and using the above C uptake rate, we estimated the storm-induced carbon production during the open water season over the full 70-yr period (Fig. 14). Again, this represents an upper bound. Since this quantity depends both on the length and number of open water storms, it is not simply dictated by the annual number of upwelling events but contains independent variability. For example, the enhanced productivity during the 1960s stands out, which is due to the large number of events in the early part of the decade and the longer-lasting storms late in the decade. Nonetheless, much of the long-term variation in productivity reflects the trends in storm count, such as the enhancement in carbon uptake over the last two decades. Included in Fig. 14 is the level of production estimated from Hill and Cota's (2005) observed growth rates (in the absence of storms) on the Chukchi slope for the open water season. This value is a bit less than the 70-year average of productivity resulting from upwelling (2800 mmol/m^2). This supports the notion that storm-driven primary production could be significant for this region, particularly over the last two decades.

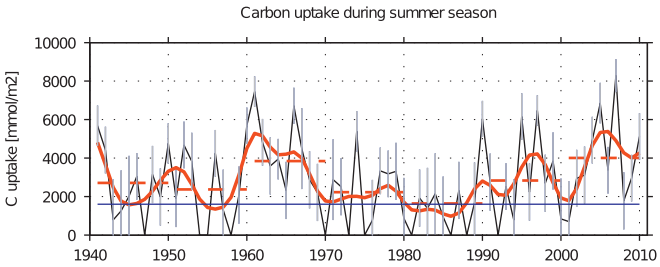

Fig. 14. Average carbon uptake (black curve) and the 7-yr lowpass (red curve) for the open water period during each year. The red dashed lines denote the decadal averages. The grey vertical lines indicate the standard error. The blue line shows the observed month-long C uptake during summer 2002 in the absence of storms (Hill and Cota, 2005). (For interpretation of the references to color in this figure legend, the reader is referred to the web version of this article.)

5. Discussion

The results presented here indicate that, while upwelling in the Alaskan Beaufort Sea is common, it is subject to pronounced seasonal, interannual, and decadal variation. Some of this is related to the large-scale atmospheric circulation patterns over the North Pacific and Western Arctic. For example, the increase in upwelling frequency in autumn is largely driven by the intensification of the Aleutian Low, while the enhancement of upwelling in the spring is partly caused by a change in location of the Aleutian Low in conjunction with the seasonal magnification of the Beaufort High. This demonstrates that complex factors dictate the characteristics of upwelling along the North Slope of Alaska. As such, more work will be necessary to sort out the relative roles of the different atmospheric phenomena, including the interplay between the two centers of action (the Aleutian low and Beaufort High). It is predicted that, under a warming climate, high latitude storms will increase in frequency and intensity (e.g. Zhang et al., 2004; Sorteberg and Walsh, 2008), which could explain in part the increase in upwelling occurrence and strength observed over the past two decades. However, it remains to be seen if the recent upwelling trends are simply part of a long-term oscillation (e.g. Polyakov et al., 2003), or whether anthropogenic change is playing a role (e.g. Moore, 2012).

Our calculations suggest that upwelling along the Alaskan Beaufort slope effectively taps nutrients from the upper halocline that can spur primary production in the euphotic zone during late-summer and early-fall, consistent with measurements in the Canadian Beaufort Sea (Tremblay et al., 2011). This is later than the normal open water bloom and has the potential to result in as much carbon uptake as that taking place earlier in the season. As the pack-ice continues to melt earlier and freeze later, there may be strong consequences for the ecosystem due to the upwelling. For example, until now the springtime peak in upwelling frequency has typically occurred when there is significant ice cover, prohibiting blooms from developing. However, it appears that due to the warming climate, as the ice thins and/or melt ponds become extensive enough in spring, this can result in early-season under-ice blooms (e.g. Arrigo et al., 2012). This implies that the spring peak in upwelling may promote even more carbon production in the years to come, with consequences for the benthos as well as for the higher trophic levels.

Acknowledgments

The authors wish to thank Victoria Hill for sharing her productivity data. They also thank Ken Brink, Glen Gawarkiewicz,

Luc Rainville, Laurie Padman, Dean Stockwell, and Jeremy Mathis for helpful discussions during the course of the study. Jia Wang provided the timeseries of the Dipole Anomaly. The following grants provided support for this study: National Aeronautics and Space Agency project NNX10AF42G (RP, KA, GD); the Natural Sciences and Engineering Research Council of Canada (KM); Bureau of Ocean Energy Management projects M09AC15207 and M10PC00116 (SD); the Year in Industry Program at the University of East Anglia (LS).

References

Arrigo, K.R., van Dijken, G., Pabi, S., 2008. Impact of shrinking Arctic ice cover on marine primary production. Geophys. Res. Lett., 35, http://dx.doi.org/10.1029/2008GL035028.

Aagaard, K., Roach, A.T., 1990. Arctic ocean-shelf exchange: measurements in Barrow Canyon. J. Geophys. Res. 95, 18,163–18,175.

Arrigo, K.R, Perovich, D.K., Pickart, R.S., 2012. Massive phytoplankton blooms under Arctic sea ice. Science 336, 1408.

Ashjian, C.J., Braund, S.R., Campbell, R.G., George, J.C., Kruse, J., Maslowski, W., Moore, S.E., Nicolson, C.R., Okkonen, S.R., Sherr, B.F., Sherr, E.B., Spitz, Y.H., 2010. Climate variability, oceanography, bowhead whale distribution, and inupiat subsistence whaling near Barrow, Alaska. Arctic 63 (2), 179–194.

Atlas, E.L., S.W. Hager, L.I. Gordon, P.K. Park, 1971. A Practical Manual for Use of the Technicon AutoAnalyzer in Seawater Nutrient Analyses Revised. Technical Report 215, 71-22, 49, Oregon State University, Department of Oceanography.

Bourgault, D., Hamel, C., Cyr, F., Tremblay, J.-E., Galbraith, P.S., Dumont, D., Gratton, Y., 2011. Turbulent nitrate fluxes in the Amundsen Gulf during ice-covered conditions. Geophys. Res. Lett., 38, http://dx.doi.org/10.1029/2011GL047936.

Carmack, E.C., Kulikov, E.A., 1998. Wind-forced upwelling and internal Kelvin wave-generation in Mackenzie Canyon, Beaufort Sea. J. Geophys. Res. 96 (21) 989–22,008.

Favorite, F., Dodimead, A.J., Nasu, K., 1976. Oceanography of the subarctic Pacific region, 1962–1972. Bull. Int. North Pac. Commission 33, 1–187.

Ghil, M., Allen, M.R., Dettinger, M.D., Ide, K., Kondrashov, D., Mann, M.E., Robertson, A.W., Saunders, A., Tian, Y., Varadi, F., Yiou, P., 2002. Advanced spectral methods for climatic time series. Rev. Geophys. 40 (1), http://dx.doi.org/10.1029/2000RG000092.

Gordon, L.I., J.C. Jennings, A.A. Ross, J.M. Krest, 1992. A Suggested Protocol for Continuous Flow Automated Analysis of Seawater Nutrients in the WOCE Hydrographic Program and the Joint Global Ocean Fluxes Study. Grp. Tech Rpt 92-1, OSU College of Oceanography Descr. Chem Oc.

Grebmeier, J.M., 1993. Studies of pelagic-benthic coupling extended onto the Soviet continental shelf in the northern Bering and Chukchi Seas. Cont. Shelf Res. 13, 653–668.

Grebmeier, J.M., 2012. Shifting patterns of life in the Pacific Arctic and Sub-Arctic seas. Ann. Rev. Mar. Sci. 4, 63–78.

Hager, S.W., Atlas, E.L., Gordon, L.I., Mantyla, A.W., Park, P.K., 1972. A comparison at sea of manual and autoanalyzer analyses of phosphate, nitrate, and silicate. Limnol. Oceanogr. 17, 931–937.

Hansell, D.A., Whitledge, T.E., Goering, J.J., 1993. Patterns of nitrate utilization and new production over the Bering-Chukchi shelf. Cont. Shelf Res. 13, 601–628.

Hill, V., Cota, G., 2005. Spatial patterns of primary production on the shelf, slope and basin of the Western Arctic in 2002. Deep Sea Res. Part II 52, 3344–3354, http://dx.doi.org/10.1016/j.dsr2.2005.10.001.

Hill, V., Cota, G., Stockwell, D., 2005. Spring and summer phytoplankton communities in the Chukchi and Eastern Beaufort Seas. Deep Sea Res. Part II 52, 3369–3385.

Janowitz, G.S., Pietrafesa, L.J., 1980. A model and observations of time-dependent upwelling over the mid-shelf and slope. J. Phys. Oceanogr. 10, 1574–1583.

Kalnay, E, Kanamitsu, M., Kirtler, R., Collins, W., Deaven, D., Gandin, L., Iredell, M., Saha, S., White, G., Woollen, J., Zhu, Y., Chelliah, M., Ebisuzaki, W., Higgins, W., Janowiak, J., Mo, K.C., Ropelewski, C., Wang, J., Leetma, A., Reynolds, R., Jenne, R., Joseph, D., 1996. The NCEP-NCAR 40-year reanalysis project. Bull. Amer. Meteorol. Soc. 77, 437–471.

Kasper, J.L., Weingartner, T.J., 2012. Modeling winter circulation under landfast ice: the interaction of winds with landfast ice. J. Geophys. Res. —Oceans 117, C04006, http://dx.doi.org/10.1029/2011JC007649.

Kerouel, R., Aminot, A., 1997. Fluorometric determination of ammonia in sea and estuarine waters by direct segmented flow analysis. Mar. Chem. 57 (3-4), 265–275.

Markus, T., Stroeve, J.C., Miller, J., 2009. Recent changes in Arctic sea ice melt onset, freezeup, and melt season length. J. Geophys. Res. 114, C12024, http://dx.doi.org/10.1029/2009JC005436.

Mathis, J.T., Pickart, R.S., 2012. Storm-induced upwelling of high pCO_2 waters onto the continental shelf of the Western Arctic Ocean and implications for carbonate mineral saturation states. Geophys. Res. Lett. 39, L07606, http://dx.doi.org/10.1029/2012GL051574 2012.

McPhee, M.G., 1980. An analysis of pack ice drift in summer. In: Sea Ice Processes and Models, edited by R. S. Pritchard, pp 62-75, Univ. of Wash. Press, Seattle, WA.

Mesquita, MDS, Atkinson, DE., Hodges, KI, 2010. Characteristics and variability of storm tracks in the North Pacific, Bering Sea, and Alaska. J. Clim., 23, http://dx.doi.org/10.1175/2009JCLI3019.1.

Moore, G.W.K., 2003. Gale force winds over the Irminger Sea to the East of Cape Farewell Greenland. Geophys. Res. Lett. 30, 184–187.

Moore, G.W.K., 2012. Decadal variability and a recent amplification of the summer Beaufort Sea High. Geophys. Res. Lett. 39, L10807, http://dx.doi.org/10.1029/2012GL051570.

Nikolopoulos, A., Pickart, R.S., Fratantoni, P.S., Shimada, K., Torres, D.J., Jones, E.P., 2009. The western Arctic boundary current at 152°W: structure, variability, and transport. Deep Sea Res. Part II 56, 1164–1181, http://dx.doi.org/10.1016/j.dsr2.2008.10.014.

Okkonen, S.R., Ashjian, C.J., Campbell, R.G., Maslowski, W., Clement-Kinney, J., Potter, R., 2009. Intrusion of warm Bering/Chukchi waters onto the shelf in the western Beaufort Sea. J. Geophys. Res. 114, C00A11, http://dx.doi.org/10.1029/2008JC004870.

Pabi, S., van Dijken, G.L., Arrigo, K.R., 2008. Primary production in the Arctic Ocean, 1998-2006. J. Geophys. Res. 113, http://dx.doi.org/10.1029/2007JC004578.

Pickart, R.S., 2000. Bottom boundary layer structure and detachment in the shelfbreak jet of the Middle Atlantic Bight. J. Phys. Oceanogr. 30 (11), 2668–2686.

Pickart, R.S., Torres, D.J., Clarke, R.A, 2002. Hydrography of the Labrador Sea during active convection. J. Phys. Oceanogr. 32, 428–457.

Pickart, R.S., Moore, G.W.K., Torres, D.J., Fratantoni, P.S., Goldsmith, R.A., Yang, J., 2009a. Upwelling on the continental slope of the Alaskan Beaufort Sea: storms, ice, and oceanographic response. J. Geophys. Res. 114, C00A13, http://dx.doi.org/10.1029/2008JC005009.

Pickart, R.S., Moore, G.W.K., Macdonald, A.M., Renfrew, I.A., Walsh, J.E., Kessler, W.S., 2009b. Seasonal evolution of aleutian low pressure system: implications for the North Pacific subpolar circulation. J. Phys. Oceanogr. 39, 1317–1339, http://dx.doi.org/10.1175/2008JPO3891.1.

Pickart, R.S., P.S. Fratantoni, (2011), Wind-forced upwelling in Barrow Canyon: transport of Pacific and Atlantic water masses. In: Proceedings of the 11th AMS Conference on Polar Meteorology and Oceanography.

Pickart, R.S., Spall, M.A., Moore, G.W.K., Weingartner, T.J., Woodgate, R.A., Aagaard, K., Shimada, K., 2011. Upwelling in the Alaskan Beaufort Sea: atmospheric forcing and local versus on-local response. Prog. Oceanogr. 88, 78–100.

Pickart R.S., M.A., Spall, J.T. Mathis., 2013. Dynamics of upwelling in the Alaskan Beaufort Sea and associated shelf-basin fluxes, Deep Sea Res. Part I, 76, 35–51.

Polyakov, I.V., Bekryaev, R.V., Alekseev, G.V., Bhatt, U.S., Colony, R.L., Johnson, M.A., Maskshtas, A.P., Walsh, D., 2003. Variability and trends of air temperature and pressure in the maritime Arctic, 1875–200. J. Clim. 16, 2067–2077.

Proshutinsky, A., Johnson, M., 1997. Two circulation regimes of the wind-driven Arctic Ocean. J. Geophys. Res. 102, 12493–12514.

Proshutinsky, A., Krshfield, R., Timmermans, M.L., Toole, J., Carmack, E., McLaughlin, F., Williams, W.J., Zimmermann, S., Itoh, M., Shimada, K., 2009. Beaufort Gyre freshwater reservoir: state and variability from observations. J. Geophys. Res. 114, C00A10, http://dx.doi.org/10.1029/2008JC005104.

Reed, R.J., Kunkel, B.A., 1960. The Arctic circulation in summer. J. Atmos. Sci. 17 (5), 489–506.

Rodionov, S.N., Overland, J.E., Bond, N.A., 2005. Spatial and temporal variability of the Aleutian climate. Fish. Oceanogr. 14, 3–21.

Sambrotto, R.N., Goering, J.J., McRoy, C.P., 1984. Large yearly production of phytoplankton in the western Bering Sea. Science 225, 1147–1155.

Schulze, L.M., Pickart, R.S., 2012. Seasonal variation of upwelling in the Alaskan Beaufort Sea: impact of sea ice cover. J. Geophys. Res. —Oceans 117, C06022, http://dx.doi.org/10.1029/2012JC007985.

Serreze, M.C., Barrett, A.P., 2011. Characteristics of the Beaufort Sea high. J. Clim. 24, 159–182, http://dx.doi.org/10.1175/2010JCLI3636.1.

Sorteberg, A., Walsh, J.E., 2008. Seasonal cyclone variability at 70 degrees N and its impact on moisture transport into the Arctic. Tellus Ser. A 60, 570–586, http://dx.doi.org/10.1111/j.1600-0870.2008.00314.x.

Spall, M.A., Pickart, R.S., Fratantoni, P.S., Plueddemann, A.J., 2008. Western Arctic shelfbreak eddies: formation and transport. J. Phys. Oceanogr. 38, 1644–1668.

Thompson, D.W.J., Wallace, J.M, 1998. The Arctic oscillation signature in the wintertime geopotential height and temperature fields. Geophys. Res. Lett. 25, 1297–1300, http://dx.doi.org/10.1029/98GL00950.

Tremblay, J.-E., Belanger, S., Barber, D.G., Asplin, M., Martin, J., Darnis, G., Fortier, L., Gratton, Y., Link, H., Archambault, P., Sallon, A., Michel, C., Williams, W.J., Philippe, B., Gosselin, M., 2011. Climate forcing multiplies biological productivity in the coastal Arctic Ocean. Geophys. Res. Lett., 38, http://dx.doi.org/10.1029/2011GL048825.

Trenberth, K.E., Hurrell, J.W., 1994. Decadal atmosphere-ocean variations in the Pacific. Clim. Dyn. 9, 303–319.

von Appen, W., Pickart, R.S., 2012. Two configurations of the Western Arctic Shelfbreak Current in Summer. J. Phys. Oceanogr., 42, http://dx.doi.org/10.1175/JPO-D-11-026.1.

Walkusz, W., Williams, W.J., Harwood, L.A., Moore, S.E., Stewart, B.E., Kwasniewski, S., 2012. Composition, biomass and energetic content of biota in the vicinity of feeding bowhead whales (Balaena mysticetus) In the Cape Bathurst upwelling region (south eastern Beaufort Sea). Deep Sea Res. Part I 69, 25–35.

Walsh, J.E., 1978. Temporal and spatial scales of Arctic circulation. Mon. Weather Rev. 106, 1532–1544.

Wang, J, Zhang, J., Watanabe, E., Ikeda, M., Mizobata, K., Walsh, J.E., Bai, X., Wu, B., 2009. Is the dipole anomaly a major driver to record lows in Arctic summer sea ice extent? Geophys. Res. Lett., 36, http://dx.doi.org/10.1029/2008GL036706.

Wilson, J.G., J.E. Overland, 1986. Meteorology of the Northern Gulf of Alaska, in The Gulf of Alaska: Physical Environment and Biological Resources, edited by D.W. Hood and S. T. Zimmerman, pp. 31–54, U. S.

Yang, J., 2006. The seasonal variability of the Arctic Ocean Ekman Transport and its role in the mixed layer heat and salt fluxes. J. Clim. 19, 5366–5387.

Zhang, X., Walsh, J.E., Zhang, J., Bhatt, U.S., Ikeda, M., 2004. Climatology and interannual variability of Arctic cyclone activity: 1948–2002. J. Clim. 17, 2300–2317.

Zimmermann, S., McKee, T., 2004. HLY-04-04 SBI Mooring Cruise. 2 Sep–1 Oct, 2004 CTD and Water Sampling Summary, Woods Hole Oceanographic Data Report.